processes

MDPI

Article

Effect of Different Voltage Frequencies of Plasma Actuators on Wind Turbine Blade Lift and Rudder Efficiency

Junjie Xu [1], Jian Zhao [2] and Jianlong Chang [1,*]

[1] College of Mechatronics Engineering, North University of China, Taiyuan 030051, China; x1239297433@163.com
[2] Jinxi Industrial Group Co., Ltd., Taiyuan 030027, China; jianqinxindan@gmail.com
* Correspondence: changjl@nuc.edu.cn

Abstract: In the field of renewable energy, wind power generation is developing rapidly. How to effectively improve the lift performance of wind turbine blades has become an urgent problem. For this reason, a plasma actuator is introduced in this paper to enhance the lift of wind turbine blades, which opens up a new path to solve this dilemma. The impact of plasma actuators with different voltage frequencies on the lift and rudder efficiency of wind turbine blades are explored in this study. Then, the flow control implications of the actuators for the airflow near the rudder are analyzed in detail. It is found that when the plasma actuator is applied to the leading edge of the rudder, the lift and rudder efficiency of the blade improve at both 0° and 15° angles of attack with increasing voltage frequency, but the effects differ significantly. At 0°, the airflow is simpler, the actuator's control effect is more pronounced, and the rudder efficiency shows a decreasing trend as the rudder reflection angle increases. In contrast, at 15°, due to complex airflow, the actuator's control capability is weaker, leading to irregular changes in rudder efficiency.

Keywords: plasma actuator; rudder efficiency; flow control; lift enhancement; vortex

check for updates

Academic Editors: Omar Dario Lopez Mejia and Santiago Lain

Received: 8 March 2025
Revised: 25 March 2025
Accepted: 28 March 2025
Published: 31 March 2025

Citation: Xu, J.; Zhao, J.; Chang, J. Effect of Different Voltage Frequencies of Plasma Actuators on Wind Turbine Blade Lift and Rudder Efficiency. *Processes* **2025**, *13*, 1032. https://doi.org/10.3390/pr13041032

Copyright: © 2025 by the authors. Licensee MDPI, Basel, Switzerland. This article is an open access article distributed under the terms and conditions of the Creative Commons Attribution (CC BY) license (https://creativecommons.org/licenses/by/4.0/).

1. Introduction

Energy is crucial to national development, and it is imperative to conserve energy today [1–3]. In the past, the burning of oil, coal, and natural gas was the main way to obtain electricity. However, their reserves are limited, and their burning polluted the atmosphere. With the advancement of technology, wind power has emerged as a renewable and clean way of generating electricity [4,5]. The aerodynamic performance of wind turbine blades, as the core of wind turbines, directly affects the efficiency of power generation, and it is of great significance to study the lift performance of blades [6]. However, the effect of simply changing the blade shape to improve the lift is limited, and there is an urgent need to find new methods. The rudder in an aircraft affects lift by changing the airflow state of the wing, and upward deflection increases the pressure difference between the top and bottom of the wing, which in turn increases the lift [7–9]. Inspired by this, the idea of introducing rudders into fan blades to assist in lifting force appeared. However, the traditional rudder has the problem of low deflection efficiency, which hinders its application in the lift enhancement of fan blades. Solving the problem of rudder inefficiency is the key to improving the lift performance of wind turbine blades and promoting the development of wind power generation technology, which is of great significance for realizing sustainable energy development [10,11].

To address the issue regarding how rudder efficiency can be enhanced, two schemes, namely active flow control and passive flow control, have been put forward from the

perspective of flow control [12–14]. A change in wind turbine blade morphology, such as a vortex generator, is usually required for passive flow control. Control can be achieved by increasing energy. However, the driving is inefficient, and flight drag is even increased. On the other hand, active flow control is characterized by a fast response speed and high control efficiency. The flow field environment in the vicinity of the rudder can be productively enhanced through it, and the flow separation phenomenon can be reduced or even prevented [15,16]. Conventional rudders with different structural shapes have different aerodynamic characteristics. For example, high-lift rudders including wedge rudders and fishtail rudders can have their lift significantly raised throughout deflection. However, at the same time, additional drag is generated by them, and the efficiency of the rudder is diminished [17]. Furthermore, the efficiency of the rudder will also be influenced by its area. As a rule, the smaller the rudder area is, the lower its efficiency will be. Meanwhile, the airflow smoothness as well as the total rudder drag are affected by rudder construction details, for example, rudder tip shape, edge configuration, and overall streamlining design, which in turn impact rudder efficiency [18].

The decline in rudder efficiency is often strongly correlated with flow separation. When the airflow from the underside of the blade is flowing to the top of the blade through the rudder gap and is mixed with it, the normal air flow on the top surface will be influenced. Therefore, significant flow separation occurs above the rudder. As a result, the pressure differential between the upper and lower surfaces narrows, and the blade's lift decreases [19]. As blade lift decreases, the overall efficiency of the rudder decreases dramatically. Consequently, the essence of solving the problem of reduced rudder efficiency lies in how the flow separation above the rudder can be eliminated or mitigated [20,21]. If the airflow can be made to flow close to the rudder, or in cases where the degree of flow separation can be controlled to reduce the size of the flow separation area, the efficiency of the rudder can be significantly enhanced. In recent years, plasma actuators, as a new active flow control technique, have been applied extensively in the field of flow control on account of their many advantages like simple structure, flexible mounting position, and fast response [22–25].

The dielectric barrier discharge plasma actuator (DBD plasma actuator) consists of three main components: the exposed electrode, the implanted electrode, and the dielectric layer. This device is widely used because of its simple structure and the thinness of the dielectric layer that can be achieved. The aerodynamic performance of blades is significantly enhanced by DBD plasma actuators. Furthermore, the structural integrity of blades is preserved due to the thin dielectric layer employed, achieving an optimal balance between aerodynamic efficiency and safety. Two main forms of voltage, namely alternating current (AC) and pulse voltage, are predominantly included in dielectric barrier discharge systems. Low-temperature induced airflow can be generated by the barrier discharge under AC voltage, which is consequently referred to as a low-temperature discharge plasma actuator. Ablation damage to turbine blades caused by high airflow temperatures is effectively prevented by this low-temperature characteristic. In contrast, high-temperature induced airflows are generated by barrier discharges at pulsed voltages, which may lead to ablative and damaging effects being caused on the blades. However, the disadvantage of AC voltage is that its induced airflow velocity is slow, and the control effect is relatively limited. Regardless, in the application of wind turbine blades, the airflow speed can still meet the practical needs, so this paper uses the AC voltage dielectric blocking discharge plasma actuator. DBD plasma actuator's mechanism is explained as follows. When the two electrodes of the actuator are connected to the high-voltage power supply, the air near the surface of the actuator is ionized, and a plasma is formed. Under the action of electric and magnetic fields, the plasma begins to move. During the motion, the plasma collides

with the surrounding gas molecules and carries out momentum transfer, thus inducing a directional motion of the gas above the actuator [26].

Currently, many scholars focus on the plasma actuator to enhance the aerodynamic performance of the blade when performing in-depth research. The core focus is on the use of plasma actuators to directly control the fluid flow state around the blade. The installation mode of the plasma actuator is modified through approaches such as series-parallel configurations and chordwise distribution adjustments [27–29]. Effective control of the blade's surrounding flow field is thereby achieved, leading to enhanced power output of the wind turbine. The dynamic stall range of the blade has been emphasized by scholars in terms of improving blade lift and optimizing aerodynamic performance [30]. By increasing the stall angle, the blade can still effectively maintain lift under the original stall angle of attack conditions. At the same time, the flow separation point of the blade is demonstrated to be significantly delayed by the plasma actuator in this study [31,32]. Consequently, the pressure difference between the upper and lower surfaces of the blade is elevated, leading to effective improvement in blade lift. Improving the aerodynamic performance of the blade is ultimately about boosting the output power of the wind turbine [33]. Through plasma actuator based flow control, significant improvements are achieved in both the self-starting capability and aerodynamic performance of wind turbines, leading to enhanced energy conversion efficiency. The active flow control methodology is demonstrated to effectively augment lift forces while simultaneously reducing drag coefficients. Existing research has primarily focused on configurations where plasma actuators are directly mounted on turbine blades. However, investigations concerning lift enhancement for blades equipped with control surfaces remain conspicuously absent in the current literature. Consequently, the development of specific solutions aimed at improving control surface efficiency is identified as an essential research direction.

To solve the problem of rudder inefficiency, the following two solutions are proposed. The first solution is that the traditional rudder structure is replaced using plasma technology. Concretely, the fluid field surrounding the blade is fulfilled to be directly controlled through plasma for the rudder. The blade's lift can be significantly raised with the application of this technology. After the roll moment generated using the maximum deflection of the aileron is compared with that on some airfoils, it has been found that the roll moment generated by the actuator even surpasses the moment caused by the aileron [34]. This demonstrated that the function of the conventional rudder can be effectively replaced by the plasma actuator. Installing the plasma actuator at the rudder's front edge in the flow separation position is the alternative, and flow control action is utilized to assist the rudder. Thus, a more significant control effect produced via the rudder deflection can be induced. By this means, the rudder deflection efficiency can be enhanced. The momentum of the blade on the rudder is directly boosted by installing a plasma actuator on it. This thus causes the blade's lift to increase at various rudder reflection angles [35,36]. In conclusion, plasma actuators are a viable option for enhancing rudder efficiency.

In this study, the second solution is adopted because it is not only applicable to a wider range of scenarios but also significantly improves the rudder efficiency while keeping the original rudder structure unchanged. In order to investigate the lift enhancement effectiveness of the plasma actuator under normal and extreme blade incoming flow conditions, 0° and 15° incoming flow angles are selected for analysis in this study. The 0° angle of attack represents the normal incoming flow condition, while the 15° angle of attack simulates the extreme situation where the turbine blades are on the verge of stalling. In this paper, with the EPPLER555 airfoil being selected as the wind turbine blade, the effects of plasma actuators with different voltage frequencies on the lift performance and rudder effectiveness of the wing under the conditions of 0° and 15° incoming flow angles

are investigated. Voltage frequency is a key determinant of plasma control capability. An increase in the voltage frequency leads to a significant augmentation in plasma density due to the increased number of discharges per unit time of the plasma actuators. The momentum exchange between the plasma and air molecules is enhanced by this change, leading to further improvement in the flow field control effect of the plasma actuator. The flow separation of the boundary layer on the surface of the wind turbine blade can be effectively suppressed with the help of high-frequency flow control technology [37]. The gas flow distribution around the blade can be optimized through this technology, resulting in altered pressure distribution on both the blade ring volume and upper/lower blade surfaces. The lift and rudder efficiency of the blade are significantly improved by these changes [35]. An in-depth investigation of the regulation mechanism of the plasma actuator in the flow field near the rudder is conducted in this paper. The control effect is modified through the adjustment of voltage frequency, which is explained in detail. The resulting influence on blade lift and rudder efficiency is then systematically analyzed.

2. Computational Model

2.1. Model and Computational Domain Grid

In this study, the numerical simulations were performed using ANSYS Fluent 2020 R2 (ANSYS Inc., Canonsburg, PA, USA). The EPPLER555 airfoil is chosen as the object of investigation, with the chord length being defined as L and the maximum thickness as 0.16 L. It is noted that the plasma actuator's momentum injection and localized heating action allow for efficient control of the flow separation. The fluid apposition time on the blade surface is prolonged, and the fluid's separation point is pushed back, which in turn improves the lift of the blade [38–40]. To ensure the actuator's better control, the actuator is mounted above the rudder at the point where flow separation occurs, which is shown in red in Figure 1. The actuator length (C) used is 0.01 times the blade length and is located 16.5 C from the aft end of the rudder. To guarantee the accuracy of the simulation data, the flow field is large enough to ensure full fluid development. Explicitly, the inlet section's radius in front of the blade is 6 L, while the length of the outflow section behind the blade is 10 L. In the computational domain, the left semicircle is set as the velocity inlet, where the velocity direction is configured at 0° and 15° to the x-axis, and the velocity magnitude is 20 m/s. Meanwhile, in the meantime, the blade part is set up as a no-slip wall, and the top, lower, and right boundaries are positioned as pressure outlets.

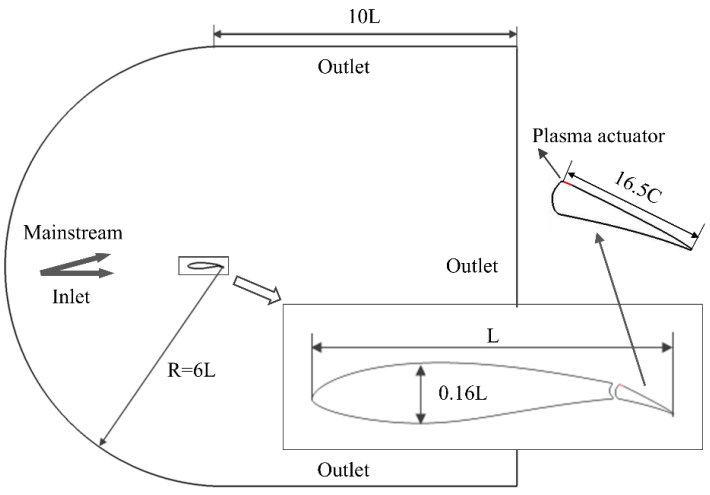


Figure 1. Flow field domain model.

The flow field mesh is an unstructured mesh, as depicted in Figure 2. In the fluid field, the grid size is progressively increased from the blade to the far-field direction. The grid size in the vicinity of the blade and in the right wake region is 1.32×10^{-5} m, while the grid size in the far-field region is expanded to 1.1×10^{-2} m. To accurately capture boundary layer flow conditions, the blade is delineated with the boundary layer mesh of 20 layers to ensure the precision of the simulation results. Meanwhile, the height of the first mesh layer on the blade surface is controlled to be 1.84×10^{-5} m, which satisfies the condition $y^+ < 1$. Meanwhile, the mesh in the wake region of the blade is encrypted to better capture the flow state of the wake of the blade.

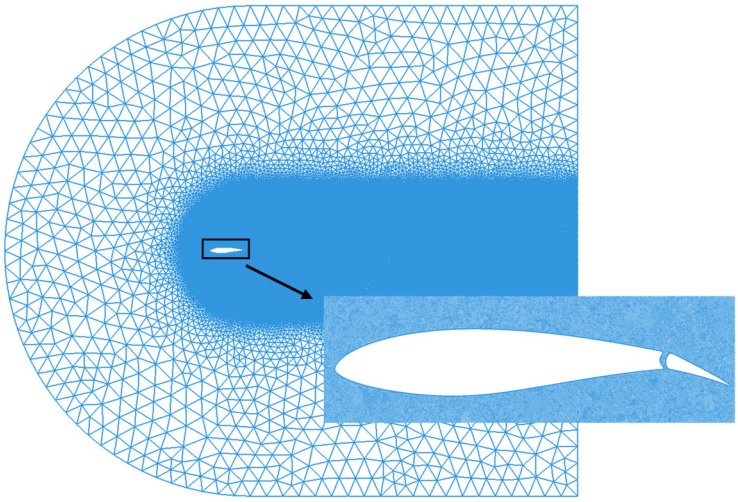


Figure 2. Computational domain mesh.

2.2. Plasma Actuator Phenomenological Model

The DBD plasma actuator discharge time is extremely short, and the specific effects of air ionization and secondary ionization on the particle motion in the flow field are not known. As a result, direct simulation of the plasma's laws of motion is not ideal because it requires an in-depth understanding of the plasma's behavioral patterns over a short period. In order to obtain a similar flow control outcome as the plasma actuator, the flow control was investigated by Shyy et al. by applying plasma excitation on a flat plate [41]. Comparing the phenomenological model with the experimental findings confirms its accuracy. Since a low-temperature plasma is produced utilizing the plasma actuator, the heat generated during plasma generation is neglected in the model. In addition, to attain control of the plasma at the macroscopic level, mean force is applied instead of particle motion. The flow control effect of the plasma is considered as an induced force, and the flow control effect of the plasma is modeled. This study's control model is derived from the phenomenological model proposed by Shyy, which is schematically revealed in Figure 3. The AOB triangular region exhibited in Figure 3 is the effective region of plasma control action, and the direction indicated by the arrow represents the direction of the electric field force, i.e., the direction of plasma movement. During directional movement, the plasma collides with neutral gas molecules, transferring momentum to them and thereby exerting a macroscopic volume force (body force) on the fluid. The body force reaches its maximum at point O and gradually decreases to its minimum along line AB. The electric field intensity at point O of the plasma actuator, denoted as E_0, represents the maximum electric field strength, while E_b signifies the cutoff electric field intensity along the sloping edge AB. In the region where the electric field strength is equal to or less than the cut-off electric field strength, it is assumed that there is no body force.

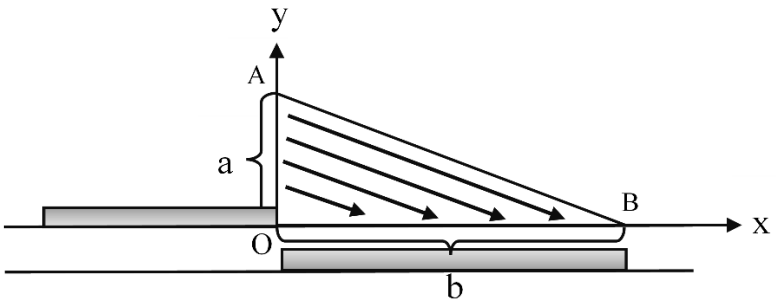


Figure 3. Schematic diagram of the working principle of the plasma actuator.

The maximum electric field strength E_0 is expressed as follows:

$$E_0 = U_0/d, \tag{1}$$

where U_0 is the maximum voltage applied between the electrodes, and d is the shortest distance between the two electrodes.

The electric field strength in the vicinity of the actuator is indicated in Equation (2).

$$|E| = E_0 - k_1 x - k_2 y, \tag{2}$$

Here, $k_1 = (E_0 - E_b)/b$, $k_2 = (E_0 - E_b)/a$.

The body force is expressed as follows:

$$F = \theta \alpha \rho_c e_c \Delta t E \delta, \tag{3}$$

where θ is the voltage frequency, ρ_c is the charge density, e_c is the charge of the charge, Δt is the electrode discharge time, E is the electric field strength vector, and $\alpha = 1$ is the elastic collision effective coefficient. In addition, $\delta = 1$ when the electric field force is greater than E_b, and $\delta = 0$ when the electric field force is less than E_b.

The vector of the electric field strength is known from the above equation as follows:

$$E = ((E \cdot k_2)/\sqrt{k_1^2 + k_2^2}, (E \cdot k_1)/\sqrt{k_1^2 + k_2^2}), \tag{4}$$

The phenomenological model of the DBD (dielectric barrier discharge) plasma actuator is the equivalent of the induced force to an electric field force that replaces the volumetric force source term in the N-S equations, thus providing flow control in the Fluent 2020 R2. Here, the continuous equation, momentum equation, and energy equations are as follows:

$$\frac{\partial \rho}{\partial t} + \nabla \cdot (\rho U) = 0, \tag{5}$$

$$\frac{\partial \rho U}{\partial t} + \nabla \cdot [\rho UU + PI] - \nabla \cdot \tau = F, \tag{6}$$

$$\frac{\partial \rho e}{\partial t} + \nabla \cdot [(\rho e + \rho)U - (U \cdot \tau) - Q_{ht}] = F \cdot U, \tag{7}$$

where U, ρ, P, e, and t are the flow velocity, fluid density, static pressure, internal energy per unit mass of fluid, and flow time, respectively. τ is the shear stress tensor, and Q_{ht} is the heat transfer term.

In Equation (6), F is the volumetric force source term of the momentum equation, i.e., the electric field force on the plasma. In Equation (7), $F \cdot U$ is the energy source term of the energy equation, i.e., the work done by the electric field force. Because of the low effect

of the energy action of the low-temperature plasma, only the momentum source term F is added into the calculation of the flow field.

2.3. Rudder Efficiency and Turbulence Modeling

Rudder efficiency is measured as the amount of moment produced when the rudder is deflected at a specific angle. On the condition that more moments can be produced by the rudder at the same angle of deflection, it is more efficient. As the model is two-dimensional, the magnitude of the roll moment can be reflected by the lift on the blade cross-section. Therefore, the lift coefficient of the blade can be measured to evaluate the rudder efficiency [42]. The rudder efficiency is expressed in Equation (8).

$$\Delta\eta = \frac{(Cl_b - Cl_0) - (Cl_a - Cl_0)}{Cl_a - Cl_0}, \tag{8}$$

Here, Cl_b is the lift coefficient generated when the rudder is deflected and the plasma actuator is applied, Cl_0 is the lift coefficient before the rudder is deflected without the plasma actuator adopted. Cl_a is the lift coefficient produced when the rudder is deflected without the plasma actuator adopted.

The Reynolds-averaged SST K-ω turbulence model is employed in this study. The fundamental principle of the SST model lies in its hybrid formulation. The K-ω model is utilized in the near-wall region, while the K-ε model is adopted at the boundary layer edge and in free shear layers. Additionally, the transport of Reynolds shear stress is incorporated through Bradshaw's hypothesis (the ratio of shear stress to turbulent kinetic energy). This formulation effectively combines the advantages of the K-ω, K-ε, and JK models. Beyond these merits, the SST model demonstrates superior capability in handling the transport of turbulent shear stresses within adverse pressure gradients and separated boundary layers. Consequently, more accurate predictions are achieved for complex flow phenomena including adverse pressure gradients and boundary layer separation.

When compared with the standard K-ω model, several enhancements are implemented in the SST K-ω formulation. Specifically, cross-diffusion originating from the ω equation is incorporated, and the turbulent viscosity is modified by the propagation of turbulent shear stresses. These improvements contribute to the enhanced accuracy and reliability of simulation results. Therefore, the SST K-ω turbulence model is selected to mitigate the effects of shear stress and complex flow conditions. The governing equations for the SST K-ω two-equation turbulence model are presented as follows:

$$\frac{\partial \vec{U}}{\partial t} + \vec{U} \cdot \nabla \vec{U} = -\nabla P + \frac{1}{Re^{2^2}}, \tag{9}$$

$$\nabla \cdot \vec{U} = 0, \tag{10}$$

The SST K-ω turbulence model equations are expressed as follows:

$$\frac{D\rho k}{Dt} = \tau_{ij}\frac{\partial U_i}{\partial x_i} - \beta^*\rho\omega k + \frac{\partial}{\partial x_j}\left[(\mu + \sigma_k\mu_t)\frac{\partial k}{\partial x_j}\right], \tag{11}$$

$$\frac{D\rho\omega}{Dt} = \frac{\gamma}{U_t}\tau_{ij}\frac{\partial U_i}{\partial x_i} - \beta\rho\omega^2 + \frac{\partial}{\partial x_j}\left[(\mu + \sigma_\omega\mu_t)\frac{\partial \omega}{\partial x_j}\right] + z, \tag{12}$$

$$z = 2\rho(1 - F_1)\sigma_{\omega 2}\frac{1}{\omega}\frac{\partial k}{\partial x_j}\frac{\partial \omega}{\partial x_j}, \tag{13}$$

where Ω is the vortex volume.

$$F_2 = \tanh(\arg_2^2), \arg_2 = \max(2\frac{\sqrt{k}}{0.09\omega y}; \frac{500U}{y^2\omega}), \tag{14}$$

Here, y is the distance from the wall, and the parameter value is detailed below:

$$\phi = F_1\phi_1 + (1 - F_1)\phi_2, \tag{15}$$

where mix function are presented as follows:

$$F_1 = \tanh(\arg_1^4), \tag{16}$$

$$\arg_1 = \min(\max(\frac{\sqrt{k}}{0.09\omega y}; \frac{500U}{y^2\omega}); \frac{4\rho\sigma_{\omega 2}k}{CD_{k\omega}y^2}), \tag{17}$$

$$CD_{K\omega} = \max(2\rho\sigma_{\omega 2}\frac{\partial k}{\partial x_j}\frac{\partial \omega}{\partial x_j}; 10^{-20}), \tag{18}$$

2.4. Model Accuracy Validation

In experimental and simulation research, the variation curves of lift coefficients were obtained by Wei et al. [43], and it is discovered that there was a significant degree of agreement between the simulation and the experimental findings. It is suggested that the flow field around the point of stall can be calculated using the LES method. To verify the accuracy of the model, the airfoil is chosen, and the same angle of rudder reflection is set for the simulation calculation. As indicated in Figure 4, our simulation results are contrasted with those of Wei et al., and the three curves are in high agreement. Thus, it can be said that this paper's approach is acceptable.

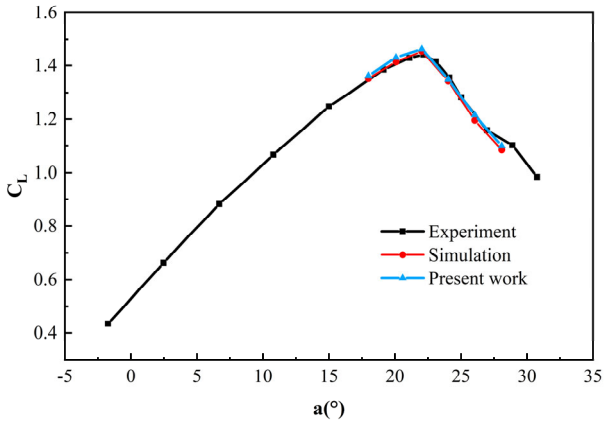


Figure 4. Comparison of lift coefficients for model accuracy validation.

To enhance computational efficiency while ensuring result accuracy, a comprehensive grid independence study is conducted. Three distinct grid configurations are systematically evaluated: Grid 1 features a minimum cell size of 3.12×10^{-5} m with 153,100 total elements; Grid 2 is refined in the blade proximity and wake regions, achieving a minimum size of 1.32×10^{-5} m in these critical zones while maintaining 582,100 elements; and Grid 3 undergoes further refinement with a 6×10^{-6} m minimum cell size around the blade and wake, coupled with enhanced far-field resolution, totaling 1,360,000 elements. The lift coefficient distributions obtained from these grid configurations are comparatively analyzed (Figure 5). It is observed that the results from Grids 2 and Grids 3 demonstrate superior agreement in lift coefficient trends when compared with Grid 1. Based on this

systematic evaluation, Grid 2 is selected as the optimal configuration, providing balanced computational accuracy and resource requirements.

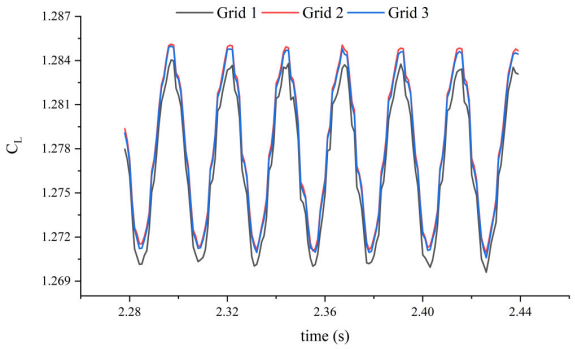


Figure 5. Comparison of lift coefficients of different mesh blades.

3. Results and Analysis

The control effectiveness of the plasma actuator is significantly influenced by the voltage frequency. On the whole, the actuator can be controlled more effectively at higher voltage frequencies. Nevertheless, in complex flow field environments, the controlling impact of the plasma may be significantly impacted. Therefore, in this study, different voltage frequency actuators are selected to investigate changing lift coefficient and rudder efficiency, due to rudder deflection under different angles of attack. Moreover, research is being performed to assess how the actuators' flow control affects the surrounding fluid field.

The Reynolds number for the study in this paper is 410,752 to determine how the lift coefficient is affected by the plasma actuator's voltage frequency, the voltage amplitude is constantly 5 kV, and the voltage frequency is set sequentially at 4 kHz, 5 kHz, 6 kHz, 7 kHz, and 8 kHz. The angle of attack, rudder deflection, and plasma actuator parameters are contained in Table 1. The angles of attack α are 0° and 15°, and the rudder deflection angles β are 3°, 4°, 5°, 6°, 7°, 8°, and 9°.

Table 1. Plasma actuator, angle of attack, and rudder deflection parameters.

Voltage Frequency	Voltage Amplitude	Angle of Attack (α)	Angle of Rudder Reflection (β)
4 kHz, 5 kHz, 6 kHz, 7 kHz, 8 kHz	5 kV	0°, 15°	3°, 4°, 5°, 6°, 7°, 8°, 9°

To facilitate the description of the parameters for the use of the plasma actuator, the following naming rule is developed. When the angle of rudder reflection is 4° and no plasma actuator is used on the rudder, the case is named 4 na (na: no actuator). As a plasma actuator with a voltage frequency of 6 kHz and a voltage amplitude of 5 kV is used on a rudder with an angle of rudder reflection of 4°, this condition is named 4a-6-5.

3.1. Effect of Actuator Voltage Frequency on Lift Coefficient

3.1.1. Effect of Voltage Frequency on Lift at $\alpha = 0°$

The average values of lift coefficients for $\alpha = 0°$ are exhibited in Table 2. It is revealed from the findings that the utilization of a plasma actuator can significantly improve the blade's lift coefficient regardless of the change in the angle of rudder reflection. Especially when the angle of rudder reflection is raised from 3° to 9°, the lift coefficient can be considerably enhanced under a voltage-frequency plasma actuator of 8 kHz. Specifically, as the rudder reflection angle is raised from 8° to 9°, just a 2.9% improvement in the lift

coefficient without the use of the actuator is obtained. Otherwise, when an 8 kHz plasma actuator is used, the lift coefficient at 9° rudder declination reaches 0.5526, which is a 19.6% lift coefficient improvement compared to that at 8° rudder declination. The influence of the actuator is most notable at β = 4°, particularly at 8 kHz. The actuator voltage frequency is 8 kHz, and the angle of rudder reflection is enhanced from 3° to 4°. The lift coefficient is prominently enhanced by about 82.7%. In contrast, the same change in the angle of rudder reflection without the plasma actuator increases the lift coefficient by only 6.2%.

Table 2. Average value of lift coefficient for α = 0°.

Voltage Frequency	β = 3°	β = 4°	β = 5°	β = 6°	β = 7°	β = 8°	β = 9°
No actuator	0.3603	0.3826	0.3959	0.4277	0.4425	0.4621	0.4755
4 kHz	0.4337	0.4606	0.4489	0.4767	0.4887	0.5045	0.5145
5 kHz	0.4654	0.4962	0.4654	0.4893	0.5009	0.5159	0.5240
6 kHz	0.5501	0.6104	0.4837	0.5029	0.5128	0.5270	0.5335
7 kHz	0.5888	0.6395	0.5058	0.5181	0.5237	0.5378	0.5428
8 kHz	0.6119	0.6583	0.5369	0.5360	0.5358	0.5494	0.5526

Without the actuator, the lift coefficient increases as the angle of rudder reflection rises. Yet, when the same voltage-frequency actuator is employed, the lift coefficients still rise with the enhancement of the angle of rudder reflection, except for a transient drop in the lift coefficient when rudder reflection angle goes up from 4° to 5°. It is further observed that the maximal value of the lift coefficient appears at β = 9°, as the voltage frequencies are 4 kHz and 5 kHz. Nevertheless, the lift coefficient reaches highest value at β = 4°, and the voltage frequency is from 6 kHz to 8 kHz. It is indicative of this phenomenon that the higher the voltage frequency is, the more effective the control of low rudder deflection. Based on this finding, by varying the actuator's voltage frequency at various rudder reflection angles, energy savings and the desired lift may be attained.

Lift coefficient curves of different voltage frequencies at α = 0° are shown in Figure 6a–f. Every 1° of rudder deflection, with or without the actuator, enhances blade lift. However, as the plasma actuator is applied, the lift is significantly elevated in contrast to the case without the actuator. In addition, the larger the voltage frequency is, the more obvious the enhancement effect of the blade lift is. Some of the lift coefficient curves remain stable with time, while some of the curves show small vibrations. This shows that the plasma actuator is not only effective in increasing the lift but also in avoiding the blade chattering problem caused by the drastic change of the lift. Upon detailed analysis of Figure 6, it can be seen that there is an abrupt rise in the lift coefficient when the voltage frequency reaches a specific value. To be specific, both the case of 4 kHz and 6 kHz frequencies result in substantial jumps in lift coefficients, when the rudder is deflected from 3° to 4°. A jump in the lift coefficient also results from the 4 kHz frequency when the rudder is deflected from 8° to 9°. Evidently, to attain the goals of a high lift coefficient and low energy consumption, voltage-frequency plasma actuators possessing these characteristics can be used.

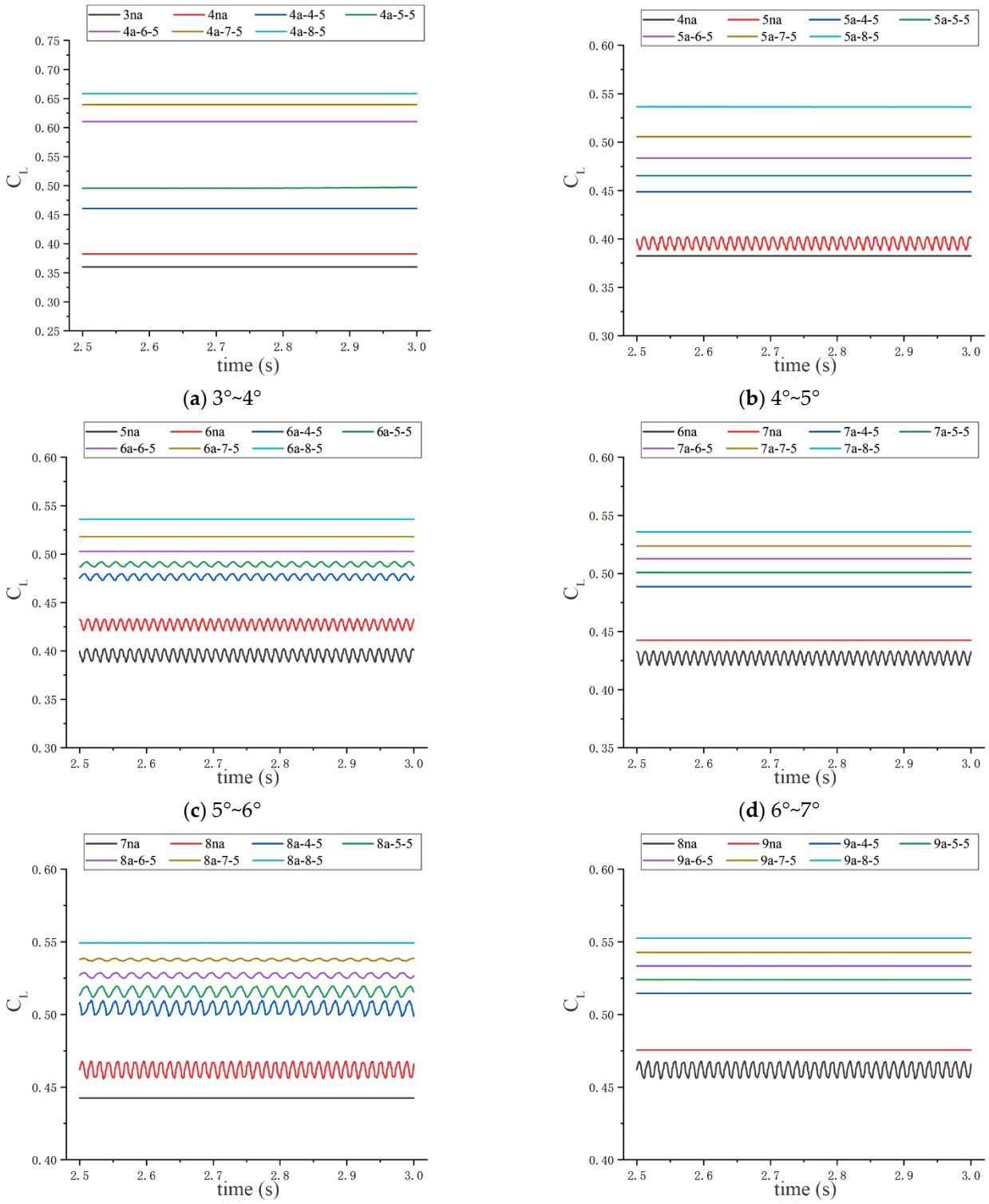


Figure 6. Lift coefficient curves of different voltage frequencies at $\alpha = 0°$.

3.1.2. Effect of Voltage Frequency on Lift at $\alpha = 15°$

Average value of lift coefficient for $\alpha = 15°$ are demonstrated in Table 3. The lift coefficient of the blade at different angles of rudder reflections is obviously enhanced through the use of actuators. In most cases, the lift coefficient increases as the voltage frequency increases. However, when $\beta = 4°$ and the voltage frequency increases from 7 kHz to 8 kHz, the lift coefficient exhibits a decrease. In addition to this special case, all

other rudder deflections adhere to this rule. Particularly at β = 8° and a voltage frequency close to 8 kHz, the plasma actuator demonstrates the optimal flow regulation efficiency. In the absence of the plasma actuator, the lift coefficient increased by merely 1.6% after the angle of rudder reflection is altered from 7° to 8°. Nevertheless, when an actuator with a frequency of 8 kHz is employed, the identical change in angle of rudder reflection leads to a 10.9% increase in the lift coefficient. To be specific, the disparity between the lift coefficients at 4 kHz and 8 kHz voltage frequencies is only 0.0124 when β = 4°. In contrast, the disparity between the lift coefficients at these two frequencies raise markedly to 0.0959 at β = 7°. It is revealed that the larger the angle of rudder reflection is, the more pronounced the effect of the enhancement in voltage frequency on the rudder efficiency. When the angle of rudder reflection increases from 8° to 9°, at the same voltage frequency, all lift coefficient averages decrease. There is also a diminish in the mean value of the lift coefficient after an increasing angle of rudder reflection. For instance, when the voltage frequency is 4 kHz and the angle of rudder reflection is increased from 5° to 6°, the average lift coefficient exhibits the same decreasing tendency. Nonetheless, the average lift coefficients are generally enhanced versus the situation without the actuator. It is obvious that the variation in the average lift coefficient is more complex and lacks a distinct regularity as the voltage frequency and angle of rudder reflection grows in comparison with the 0°angle of attack.

Table 3. Average lift coefficient values at α = 15°.

Voltage Frequency	β = 3°	β = 4°	β = 5°	β = 6°	β = 7°	β = 8°	β = 9°
No actuator	1.2589	1.2635	1.2817	1.2821	1.3021	1.3235	1.3340
4 kHz	1.2708	1.3293	1.2903	1.2879	1.3072	1.4179	1.4036
5 kHz	1.3297	1.3400	1.2926	1.3600	1.3844	1.4257	1.4117
6 kHz	1.3375	1.3484	1.3610	1.3687	1.3915	1.4328	1.4181
7 kHz	1.3456	1.3559	1.3682	1.3748	1.3979	1.4379	1.4231
8 kHz	1.3538	1.3417	1.3747	1.3798	1.4031	1.4443	1.4282

The curves of the influence of various voltage frequencies upon the lift coefficient after a 1° increase in the rudder at α = 15° are illustrated in Figure 7. It is evident that the fluctuations of all the lift coefficient curves grow in magnitude and show a cyclic variation compared to the case at α = 0°. By comparing the curves in Figure 7, three main patterns of lift coefficient curves can be concluded: delta function type, as displayed in 3 na; irregular oscillation type, as illustrated in 9 na; and oscillation delta function type, as depicted in 5a-6-7. To be specific, in Figure 7b, the curves corresponding to 5a-6-4 are of the delta function type. The formation of these three characteristic curves is intrinsically related to vortex shedding mechanisms. The delta function type curve is generated by periodic shedding of vortices with consistent intensity. When the shed vortices maintain comparable strength, the amplitude of lift coefficient fluctuations remains relatively uniform. The irregular oscillation type curve results from a non-uniform vortex strength distribution. Stronger vortices induce more pronounced lift fluctuations during shedding, while weaker vortices produce negligible effects, collectively leading to the irregular oscillatory pattern. The oscillation delta function type curve is attributed to the coexistence of high-intensity vortices with shorter shedding periods and persistent low-intensity vortex shedding. The characteristic oscillatory delta composite pattern is created by this superposition. This curve exhibits similarity to the lift coefficient curve in the case where no actuator is employed, while it notably augments the lift of the blade. The curve representing 5 na, on the other hand, belongs to the type of irregular oscillations with a smaller average fluctuation amplitude and is one of the better lift coefficient waveforms produced by the blade in the absence of plasma excitation. As for the lift coefficient curves generated by 5a-6-5,

5a-6-6, and 5a-6-7, they are of the oscillation delta function type. In this type of curve, although the amplitude of each oscillation is small, the curve of the simple delta function type has a substantially smaller variation in the highest and lowest points throughout a whole trigonometric cycle. Accordingly, the oscillatory effects of the blade can be amplified by such curves with adverse impacts. So, when selecting voltage frequencies, frequencies that may lead to the appearance of such curves should be avoided as much as possible.

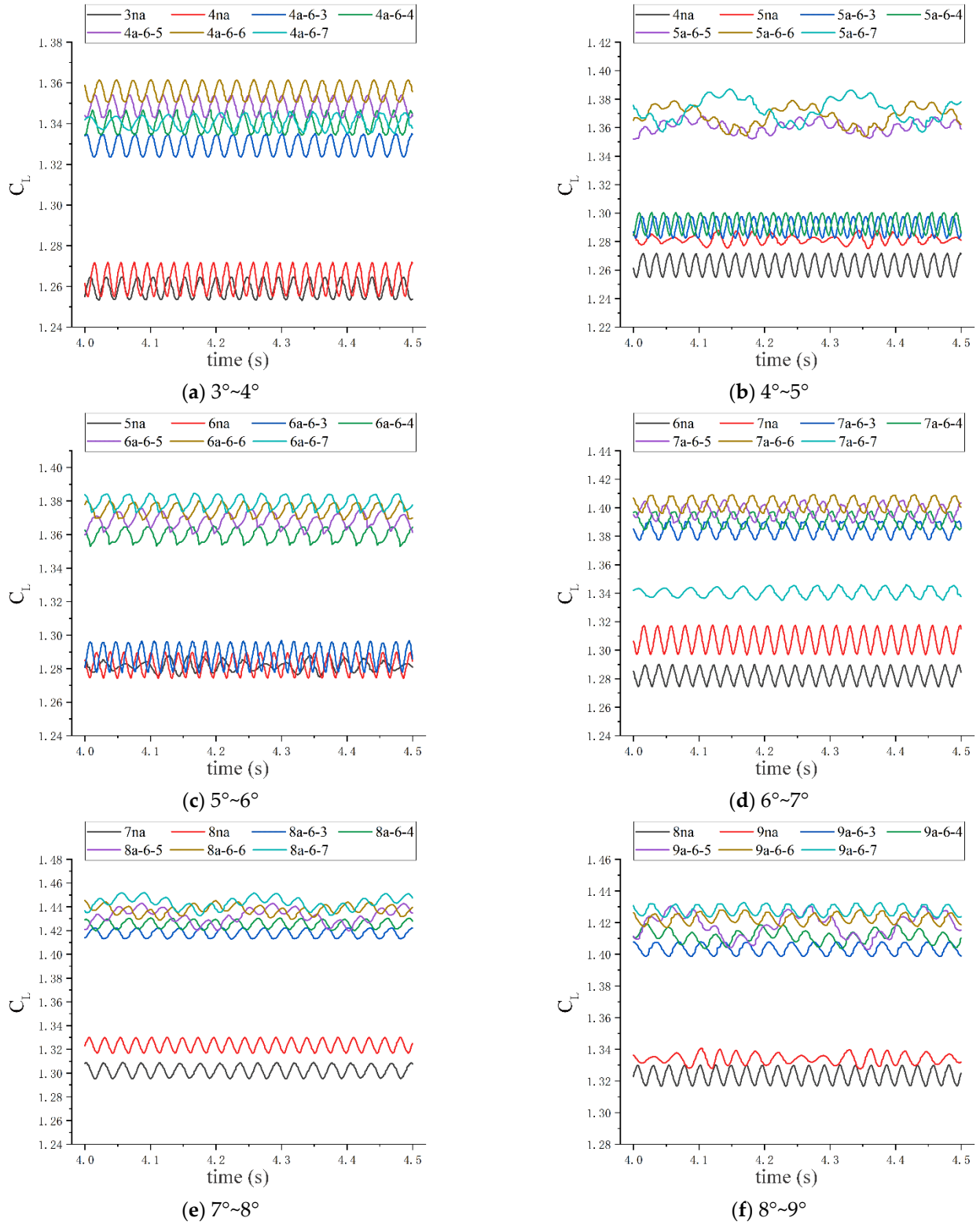


Figure 7. Lift coefficient curves of different voltage frequencies at $\alpha = 15°$.

3.2. Effect of Actuator Voltage Frequency on Rudder Efficiency

3.2.1. Effect of Voltage Frequency on Rudder Efficiency at $\alpha = 0°$

The impact of actuator on rudder efficiency at different voltage frequencies is revealed in Table 4. There is evidence that the use of a plasma actuator can have a very positive impact on the efficiency of the rudder. When the angle of rudder reflection is increased from 3° to 4°, the rudder efficiency is only 21.649% at a voltage frequency of 4 kHz. However, as the voltage frequency is increased to 8 kHz, the rudder efficiency surges to 76.52%, which is 54.871% higher than that at 4 kHz. It is illustrated that the improvement in rudder efficiency is considerably affected by the augmentation in voltage frequency. At the same voltage frequency, the larger the angle of rudder reflection is, the lower the rudder efficiency usually is. As an illustration, when the voltage frequency is 8 kHz and the rudder is deflected from 8° to 9°, the efficiency is reduced by 59.835% compared to that when the rudder is deflected from 3° to 4°. In addition, when the angle of rudder reflection is smaller, its efficiency improvement is faster while the actuator frequency is raised, and vice versa. Specifically, when the rudder is deflected from 3° to 4°, the rudder efficiency can be advanced by about 9.88% if the voltage frequency is enhanced from 4 kHz to 5 kHz. Nonetheless, when the rudder deflection is changed from 8° to 9°, the increase in rudder efficiency amounts to merely 2.056%, even though the voltage frequency is simultaneously elevated from 4 kHz to 5 kHz. Therefore, when the angle of rudder reflection is relatively small, a higher voltage frequency can be chosen to enhance efficiency. Conversely, when the angle of rudder reflection is relatively large, a lower voltage frequency should be adopted to conserve energy.

Table 4. Rudder efficiency for different voltage frequencies at $\alpha = 0°$.

Voltage Frequency	3°~4°	4°~5°	5°~6°	6°~7°	7°~8°	8°~9°
4 kHz	21.649%	13.853%	12.377%	10.802%	9.582%	8.440%
5 kHz	31.529%	18.165%	15.559%	13.654%	12.158%	10.496%
6 kHz	63.225%	22.948%	18.995%	16.437%	14.667%	12.551%
7 kHz	71.302%	28.725%	22.834%	18.985%	17.107%	14.564%
8 kHz	76.520%	36.853%	27.355%	21.814%	19.729%	16.685%

3.2.2. Effect of Voltage Frequency on Rudder Efficiency at $\alpha = 15°$

Upon comparing the data in Table 5, it is found that the actuator's rudder efficiency is substantially higher at $\alpha = 15°$ than at $\alpha = 0°$. Exactly, the maximum value of rudder efficiency is 76.52% at $\alpha = 0°$, whereas the maximum value of rudder efficiency attains 24,425% at $\alpha = 15°$, representing an increase of 24,348.48% compared with $\alpha = 0°$. It is indicated that the plasma at $\alpha = 15°$ is more effectively regulated with the actuator. At $\alpha = 0°$, the maximum value of rudder efficiency emerges when the voltage frequency is 8 kHz and the angle of rudder reflection is altered from 3° to 4°, and the rudder efficiency declines with the augmentation of the angle of rudder reflection. Nevertheless, a clear regularity is not exhibited in the impact of the angle of rudder reflection being increased or decreased on the rudder efficiency at $\alpha = 15°$. The complex flow within the flow field in the absence of the actuator's action results in an irregular variation in the rudder efficiency. Still, upon the actuator being incorporated, the efficiency of the rudder is remarkably enhanced in comparison with that without the actuator, albeit the variation of the rudder efficiency remains complex. It is suggested that an important role in improving rudder efficiency is played through plasma actuators. However, it is worthy of note that this effect fails to exhibit a distinct regularity with the augmentation of the angle of rudder reflection. In contrast, the rudder efficiency declines with the increase in the angle of rudder reflection at $\alpha = 0°$.

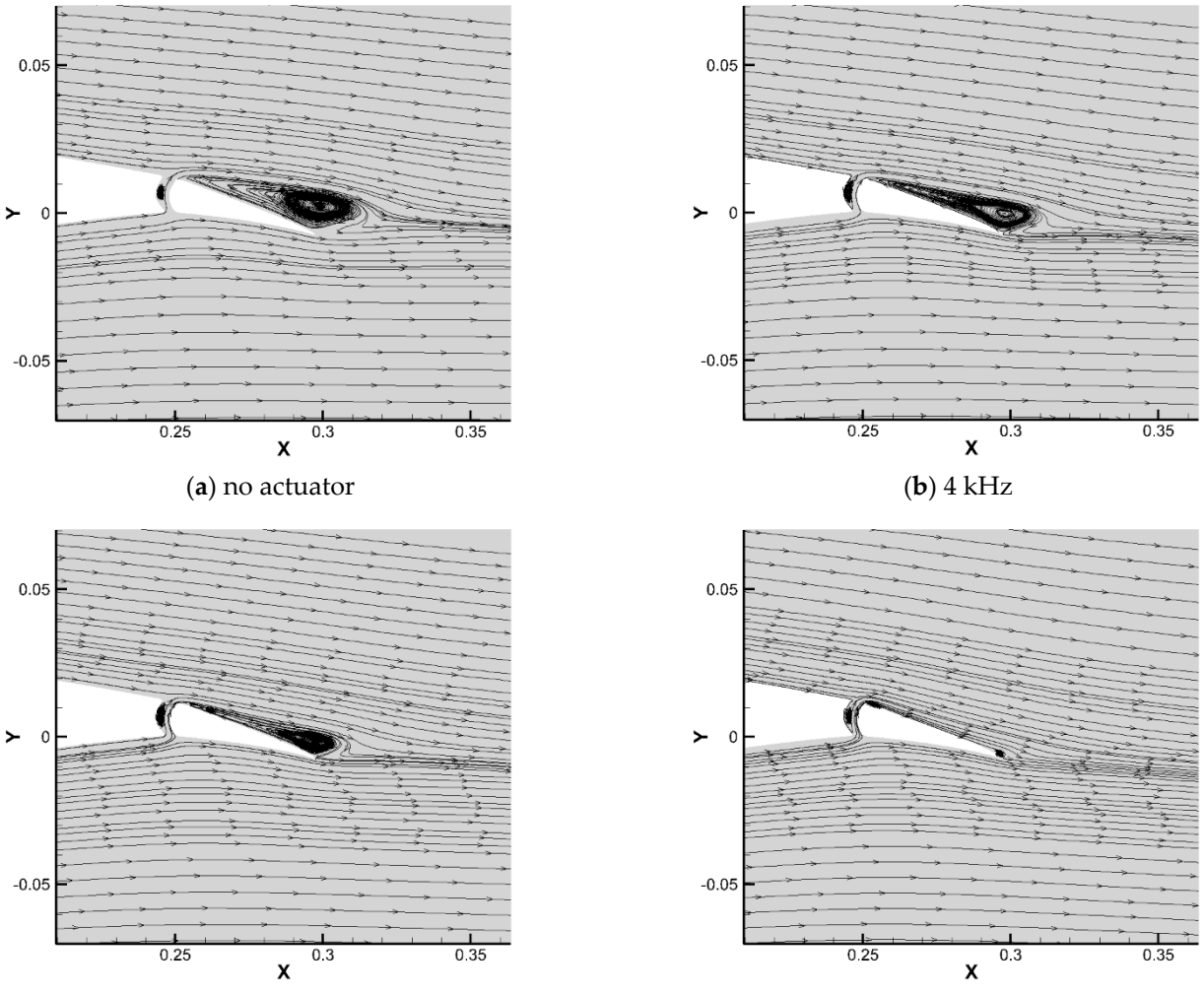
Table 5. Rudder efficiency for different voltage frequencies at α = 15°.

Voltage Frequency	3°~4°	4°~5°	5°~6°	6°~7°	7°~8°	8°~9°
4 kHz	1430%	47%	1450%	25%	441%	663%
5 kHz	1663%	60%	19475%	412%	478%	740%
6 kHz	1846%	436%	21650%	446%	509%	801%
7 kHz	2009%	475%	23175%	479%	535%	849%
8 kHz	1700%	511%	24425%	505%	564%	897%

3.3. Flow Field Analysis

3.3.1. Flow Field Analysis at α = 0°

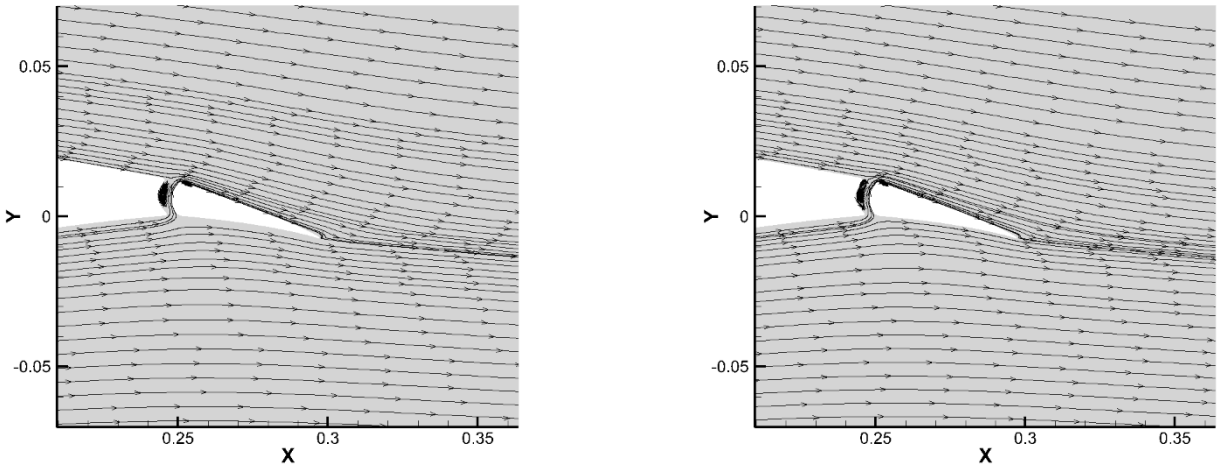
The streamlines of different voltage frequencies at α = 0° and β = 4° are presented in Figure 8. The findings show that the existence of the plasma actuator substantially raises the kinetic energy of the fluid on the rudder's upper surface. This, in turn, speeds up the fluid flow velocity and leads to the downstream movement of associated rudder vortices over the top surface. As the plasma actuator's voltage frequency grows, the area of adhering vortices is reduced, until they vanish completely at 7 kHz and 8 kHz. At this point, the gas can be made to flow closely to the upper surface of the rudder, which effectively augments the lift of the blade.



(**a**) no actuator (**b**) 4 kHz

(**c**) 5 kHz (**d**) 6 kHz

Figure 8. *Cont.*

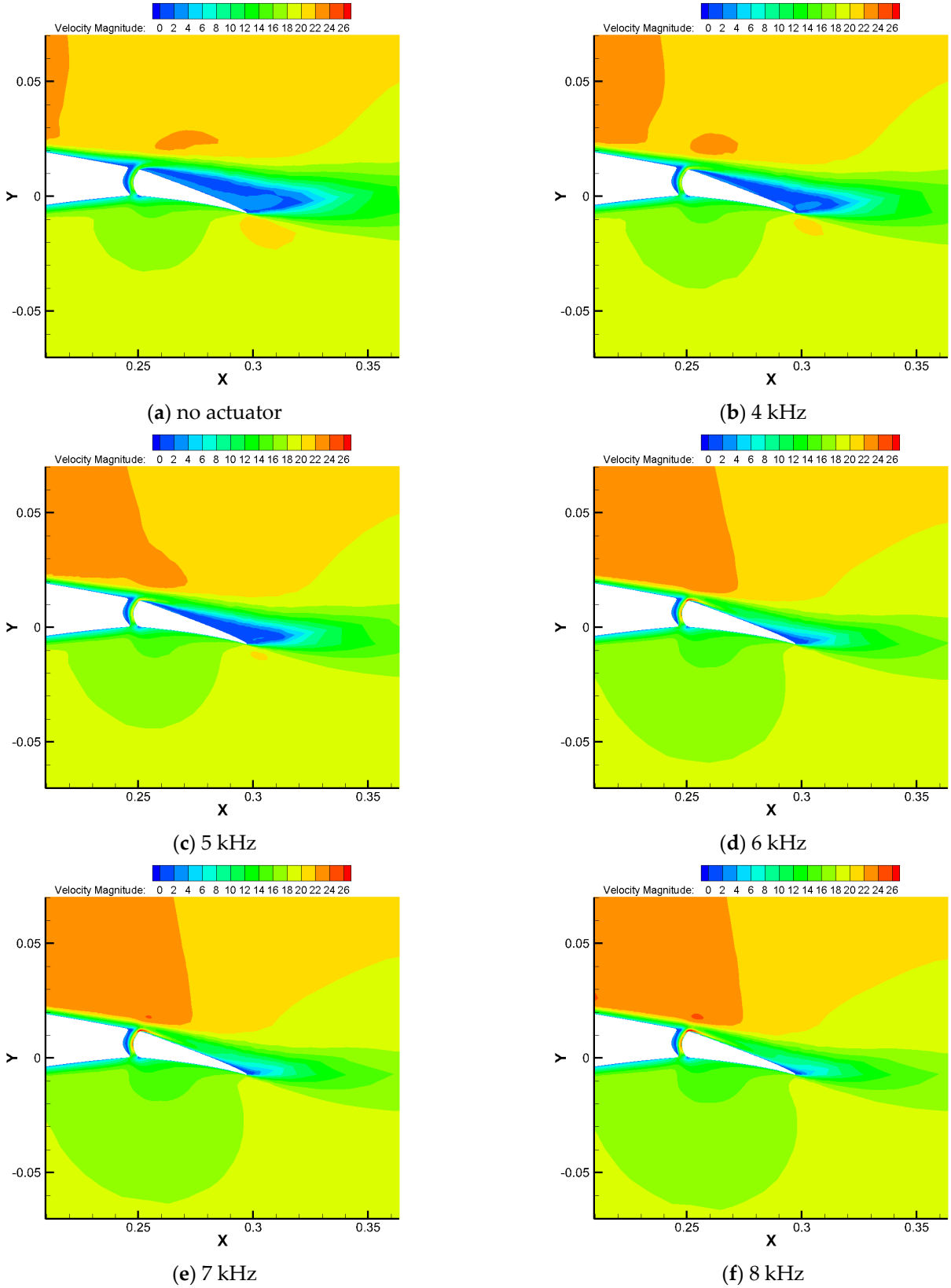


(**e**) 7 kHz (**f**) 8 kHz

Figure 8. Streamlines of different voltage frequencies at $\alpha = 0°$ and $\beta = 4°$.

As shown on Figure 9a, the flow at the front edge of the rudder is quite complex. Due to the gap between the main blade and the rudder, the airflow flowing faster on the lower surface will ascend to the top surface and interact with the fluid at top surface. Fluid detachment from the blade top surface at the rudder leading edge is caused by this interaction, which in turn produces flow separation as well as the development of huge attached vortices above the rudder. To achieve optimal flow control, the actuator is situated close to the point where the flow separates [44]. However, at voltage frequencies of 4 kHz and 5 kHz, the influence of the actuator is not visible and does not cause the fluid above the rudder to flow near the blade surface. However, the attached vortex area is significantly reduced, and the tendency of the fluid to flow near the wall surface gradually emerges with the increase in the voltage frequency. When the voltage frequency is further increased to the range of 6 kHz to 8 kHz, the generation of vortices can be clearly observed at the installation location of the plasma actuator. These vortices help to improve the energy transfer among the entering flow and the boundary layer, and the fluid is induced to flow close to the wall, which markedly improves the flow field capability to resist the backpressure gradient as well as suppress flow separation.

The velocity nephograms of different voltage frequencies at $\alpha = 0°$ and $\beta = 4°$ are illustrated in Figure 9. While in the case with no actuator, a large blue area above the rudder with a velocity lower than 8 m/s is presented. This blue area is gradually reduced as the voltage frequency of the plasma actuator rises. When the voltage frequency is 8 kHz, only a very small blue low-velocity region is visible on the rudder tail. During the operation of the plasma actuator, a high-velocity fluid is generated at the actuator installation position, and the incoming flow rate is exceeded by its flow rate, which is approximately 26 m/s. In addition, this high-velocity fluid is not only present at the front edge of the rudder, but also covers the seam area between the main blade and the rudder. When the voltage frequency of the plasma actuator increases, the area of the high-velocity fluid region will be correspondingly enlarged, and the flow velocity will also be gradually augmented, so as to achieve a better flow control effect.



(**a**) no actuator (**b**) 4 kHz

(**c**) 5 kHz (**d**) 6 kHz

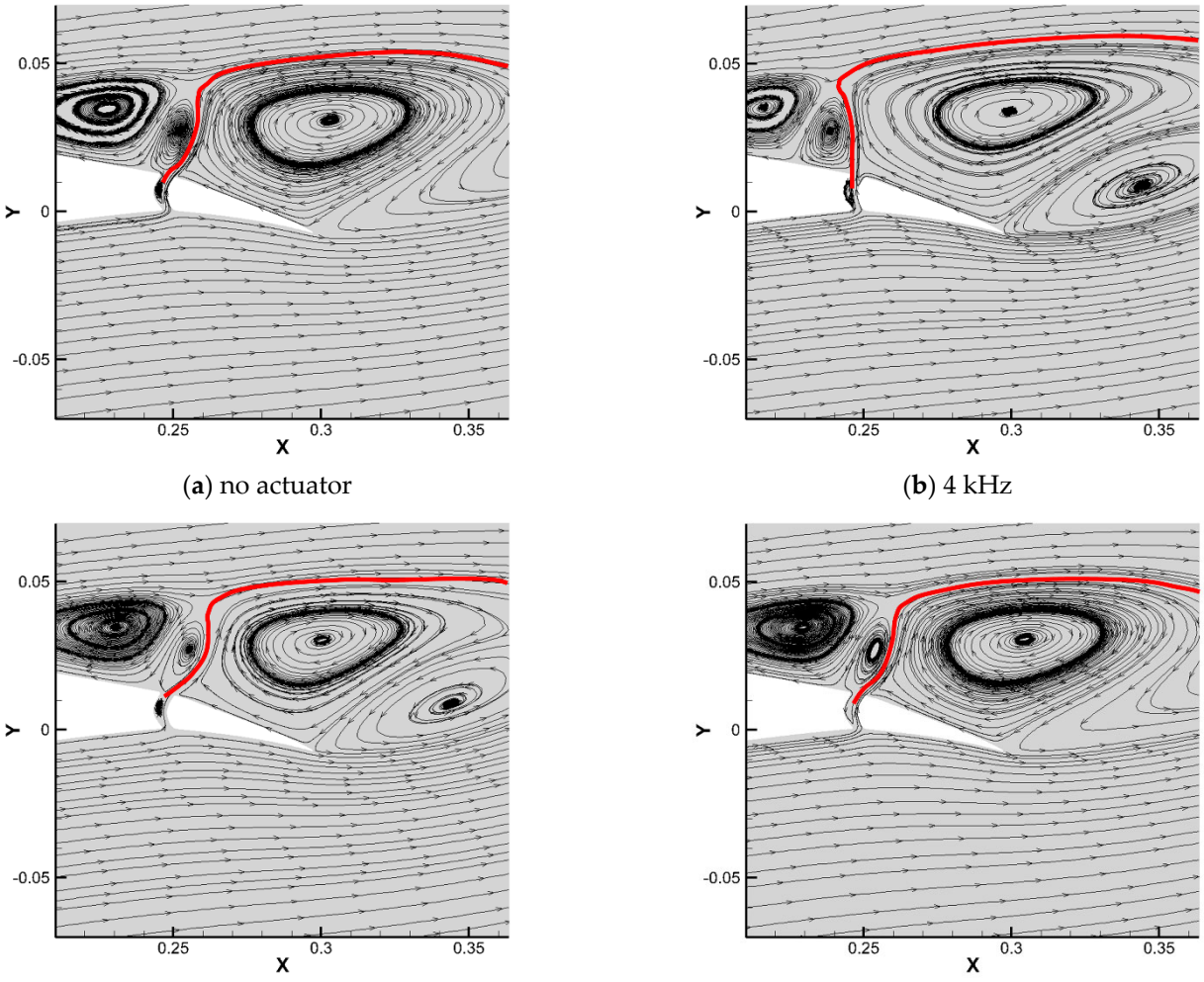
(**e**) 7 kHz (**f**) 8 kHz

Figure 9. Velocity nephograms of different voltage frequencies at $\alpha = 0°$ and $\beta = 4°$.

3.3.2. Flow Field Analysis at $\alpha = 15°$

The streamlines of different voltage frequencies at $\alpha = 15°$ and $\beta = 4°$ are depicted in Figure 10. Flow separation at the main blade is noted, and this separation persists across the entire blade. In Figure 10a–e, four vortices are generated above the blade, including the

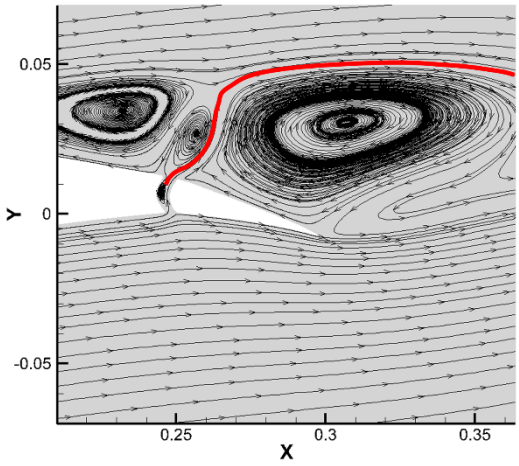
flow separation vortex above the main blade, the vortex generated by the velocity difference between blade and rudder, the vortex above rudder, and the vortex behind rudder. Under the combined effects of these vortices, the flow speed above the blade surface is reduced, and the blade's lift is significantly decreased. In Figure 10f, three vortices are generated over the blade. Among them, the flow separation vortex above the main blade shifts above the rudder, developing a vortex with a larger area. Simultaneously, the vortices above and behind the rudder progressively approach the rudder under the compression of the larger vortex, and the area of the vortex is significantly diminished. The flow trajectory of the lower edge fluid flowing from the gap to the upper edge after coupling with the upper edge fluid is shown by the red line. The angle of the red line gradually grows as the voltage frequency rises, as shown by the red line. It is indicated that an increase in voltage frequency helps the fluid flow closer to the control surface, thereby demonstrating that effective control is provided by the plasma actuator at the leading edge of the rudder. Especially in Figure 10f, a significant change is observed in the red line, indicating that the fluid is able to flow closely along the upper wall of the rudder. This indicates that the induction effect is optimized when the 8 kHz plasma actuator is employed.



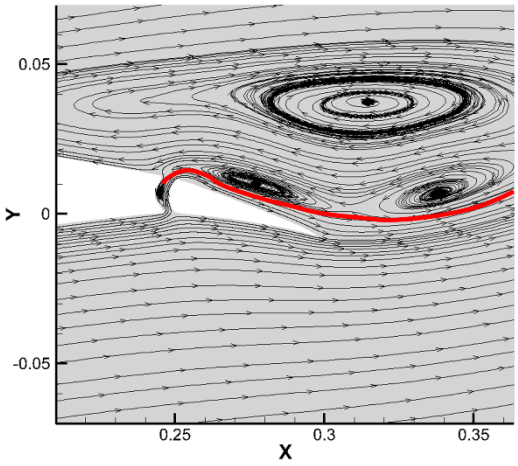
(**a**) no actuator (**b**) 4 kHz

(**c**) 5 kHz (**d**) 6 kHz

Figure 10. *Cont.*



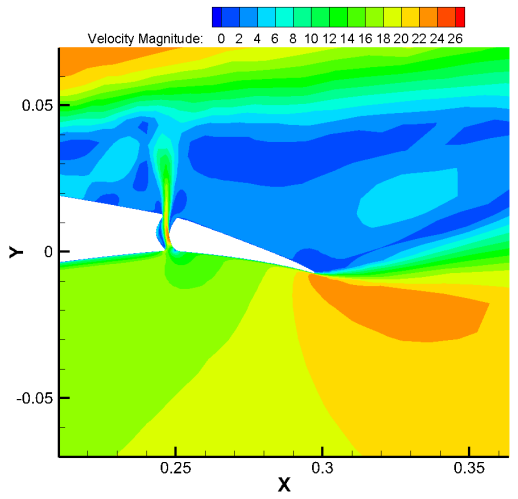
(**e**) 7 kHz



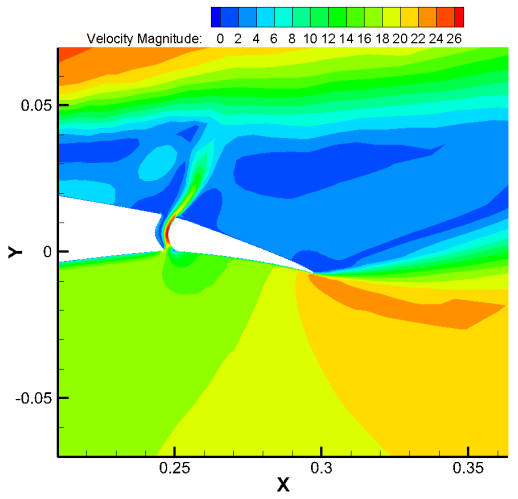
(**f**) 8 kHz

Figure 10. Streamlines of different voltage frequencies at α = 15° and β = 4°.

The velocity nephograms of different voltage frequencies at α = 15° and β = 4° are presented in Figure 11. Compared with the 0° angle, the area of the blue low-speed region is significantly increased. Large low-speed areas are formed over the rudder and main blade. The low velocity region coincides with the region where vortices are present in Figure 10, and the correlation between the decrease in fluid flow velocity and the presence of vortices is further confirmed. Simultaneously, the red area at the front edge of the rudder is markedly different from the condition at α = 0°. At α = 0°, the upper edge of the rudder is where the red portion of the actuator is stretched. However, when α = 15°, the red area is connected to the upper edge of the rudder only at 8 kHz. In other cases, the red high-velocity fluid will flow along the gap to the upper right of the blade. This indicates that the flow from the gap to the upper edge is not effectively controlled by the plasma actuator at the low voltage frequency at α = 15°. At the same time, it also further indicates that under the complex flow field conditions at α = 15°, the regulating effect of the actuator is relatively low, and the voltage frequency needs to be enhanced to resist the original flow state, which is significantly reduced compared with that at α = 0°.

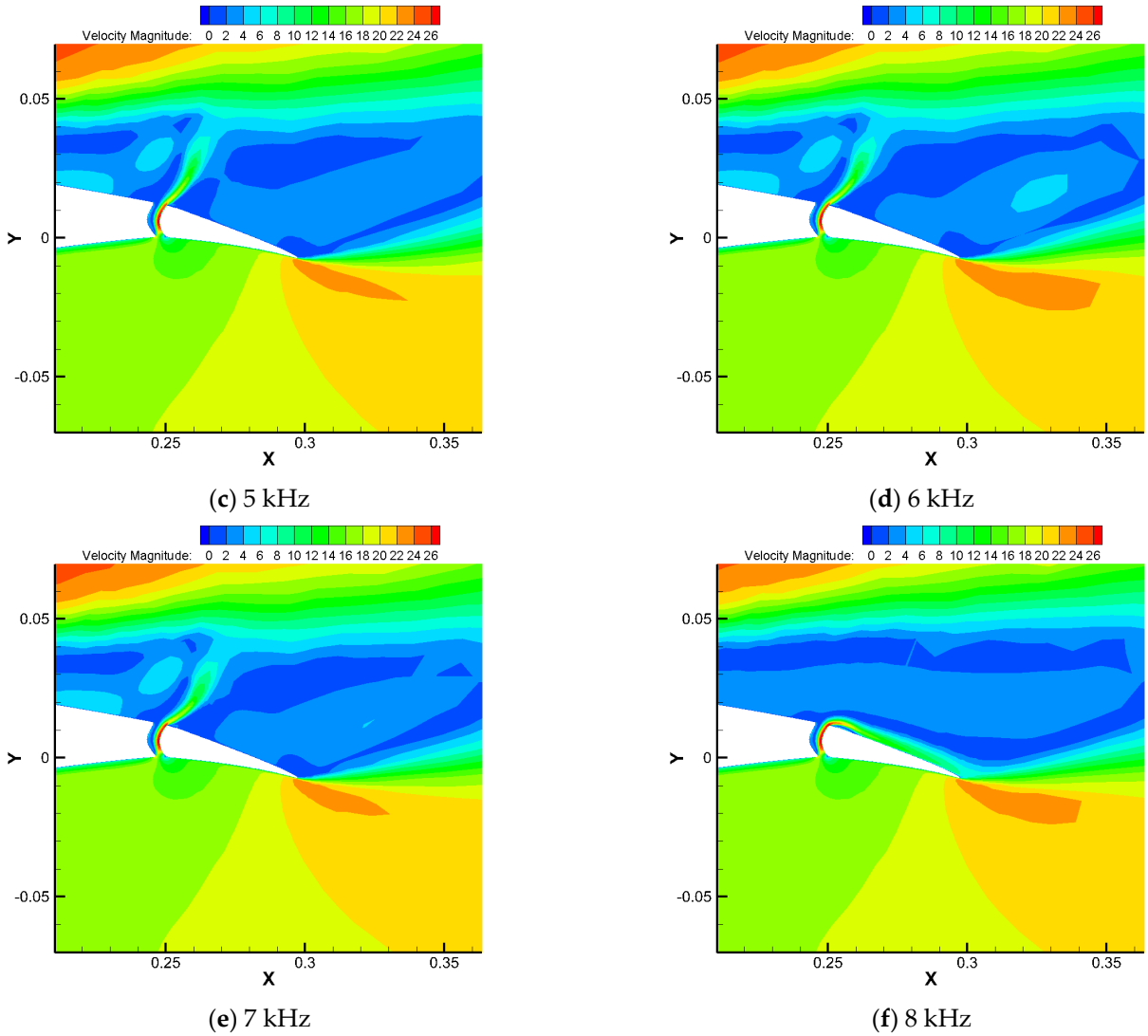


(**a**) no actuator



(**b**) 4 kHz

Figure 11. *Cont.*



(**c**) 5 kHz (**d**) 6 kHz

(**e**) 7 kHz (**f**) 8 kHz

Figure 11. Velocity nephograms of different voltage frequencies at $\alpha = 15°$ and $\beta = 4°$.

4. Conclusions

In this study, the investigations are conducted on the lift coefficients, rudder efficiency, and flow field conditions of the wind turbine blades of the EPPLER555 airfoil at different rudder deflections after being controlled with different plasma actuators at two angles of attack. The following conclusions are obtained:

(a) The lift and rudder efficiency of the blade at both 0° and 15° angles of attack can be effectively improved by the actuator, and then the efficiency of wind turbine power generation is effectively improved. The actuator's influence upon the rudder efficiency is increased as the rudder deflection angle decreases at $\alpha = 0°$. However, at $\alpha = 15°$, the complex flow of airflow around the blade leads to the fact that the enhancement effect of the actuator on the rudder efficiency does not show a regular change with the rudder deflection angle. The enhancement effect of the actuator on the rudder efficiency is amplified with the rise of the voltage frequency for both angles of attack.

(b) When $\alpha = 0°$, flow separation is only caused at the leading edge of the rudder, and only attached vortices are generated above the rudder. When $\alpha = 15°$, flow separation is caused when the airflow passes through the main blade, and multiple vortices are formed above the blade, making the flow situation more complicated. Moreover, at $\alpha = 15°$, three types of lift coefficient curves are generated by applying the plasma

actuator: delta function type, irregular oscillation type, and oscillation delta function type. To reduce the issue of blade flutter created by the drastic change in the lift coefficient, the oscillating delta function type of curve should be avoided when selecting the voltage frequency. At the same time, to accomplish high lift coefficient and low energy consumption, voltage-frequency plasma actuators with jumping characteristics can be used.

(c) As the excitation frequency of the plasma actuator grows at $\alpha = 0°$, the attached vortex area above the rudder gradually reduces. As a result, the fluid flow velocity is gradually accelerated, causing the flow to move closer to the rudder. As the excitation frequency of the plasma actuator increases at $\alpha = 15°$, the angle of the flow trajectory of the fluid flowing from the gap at the lower edge to the upper edge is gradually increased. It is indicated that the increase in the voltage frequency contributes to the fluid flow being moved closer to the rudder. Especially when the voltage frequency reaches 8 kHz, the original flow state can be effectively changed, causing the fluid to be closer to the rudder.

Author Contributions: Conceptualization, J.X. and J.C.; Data curation, J.Z.; Formal analysis, J.C.; Funding acquisition, J.C.; Investigation, J.X., J.Z. and J.C.; Methodology, J.X. and J.Z.; Project administration, J.Z.; Resources, J.X.; Software, J.X.; Supervision, J.C.; Validation, J.X., J.Z. and J.C.; Visualization, J.X.; Writing—original draft, J.X.; Writing—review & editing, J.Z. and J.C. All authors have read and agreed to the published version of the manuscript.

Funding: This research was funded by the National Natural Science Foundation of China (grant number 12202408) and the Aviation Science Foundation (grant number 2019ZA0U0001).

Data Availability Statement: The data used to support the findings of this study are available from the corresponding author (changjianlong1989@126.com) upon request.

Conflicts of Interest: Author Jian Zhao was employed by Jinxi Industrial Group Co., Ltd. The remaining authors declare that the research was conducted in the absence of any commercial or financial relationships that could be construed as a potential conflict of interest.

Abbreviations

The following abbreviations are used in this manuscript:

DBD	Dielectric barrier discharge
na	No actuator

References

1. Jureczko, M.; Mrowka, M. Multiobjective Optimization of Composite Wind Turbine Blade. *Materials* **2022**, *15*, 4649. [CrossRef] [PubMed]
2. Teng, H.; Li, S.; Cao, Z.; Li, S.; Li, C.; Ko, T.J. Carbon Fiber Composites for Large-Scale Wind Turbine Blades: Applicability Study and Comprehensive Evaluation in China. *J. Mar. Sci. Eng.* **2023**, *11*, 624. [CrossRef]
3. Zhang, Y.; Zhang, C.; You, H.; Liang, K.; Wei, C.; Sun, A. Analysis of performance improvement methods for offshore wind turbine blades affected by leading edge erosion. *Ocean Eng.* **2024**, *310*, 118773. [CrossRef]
4. Chu, Y.-J.; Lam, H.-F.; Peng, H.-Y. Numerical investigation of the power and self-start performance of a folding-blade horizontal axis wind turbine with a downwind configuration. *Int. J. Green Energy* **2022**, *19*, 28–51. [CrossRef]
5. Zhang, X.; Zheng, M. Numerical Simulation of Fluid-Structure Coupling for a Multi-Blade Vertical-Axis Wind Turbine. *Appl. Sci. Basel* **2023**, *13*, 8612. [CrossRef]
6. Yan, P.; Li, Y.; Gao, Q.; Lian, S.; Wu, Q. Design and Analysis of an Adaptive Dual-Drive Lift-Drag Composite Vertical-Axis Wind Turbine Generator. *Energies* **2023**, *16*, 7529. [CrossRef]
7. Sato, M. Passive Fault-Tolerant Flight Control Design Example for Elevator Efficiency Reduction Using Structured H∞ Control. In Proceedings of the 29th Mediterranean Conference on Control and Automation (MED), Puglia, Italy, 22–25 June 2021; pp. 627–632.

8. Kim, S.; Horspool, K.R. Nonlinear Controller Design for Non-minimum Phase Flight System Enhanced by Adaptive Elevator Algorithm. In Proceedings of the AIAA Science and Technology Forum and Exposition (AIAA SciTech), Orlando, FL, USA, 6–10 January 2020.
9. Singh, Y.; Bagri, K.; Jayakumar, A.; Rizzoni, G. Fault Diagnostics for Oscillatory Failure Case in Aircraft Elevator Servos. In Proceedings of the 22nd World Congress of the International Federation of Automatic Control (IFAC), Yokohama, Japan, 9–14 July 2023; pp. 408–415.
10. Singh, U.; Rizwan, M.; Malik, H.; Marquez, F.P.G. Wind Energy Scenario, Success and Initiatives towards Renewable Energy in India-A Review. *Energies* **2022**, *15*, 2291. [CrossRef]
11. Urabe, C.T.; Ikegami, T.; Ogimoto, K. Mitigation of Short-Term Fluctuations in Wind Power Output in a Balancing Area on the Road Toward 100% Renewable Energy. *EEE Access* **2022**, *10*, 111210–111220. [CrossRef]
12. Esmaeili, A.; Sousa, J.M.M. Combined passive and active flow control for fixed-wing micro air vehicles. *Int. J. Micro Air Veh.* **2023**, *15*, 17568293231197127. [CrossRef]
13. Gupta, S.; Kumar, S.; Kumar, R. Control of leading-edge vortices over delta wing using flow control methods: A review. In Proceedings of the 2nd International Conference on Functional Material, Manufacturing and Performances (ICFMMP), Phagwara, India, 17–18 September 2022; pp. 2189–2193.
14. Rashid, S.; Nawaz, F.; Maqsood, A.; Salamat, S.; Riaz, R. Review of wave drag reduction techniques: Advances in active, passive, and hybrid flow control. *Proc. Inst. Mech. Eng. Part G J. Aerosp. Eng.* **2022**, *236*, 2851–2884. [CrossRef]
15. Spens, A.; Pisano, A.P.; Bons, J.P. Leading-Edge Active Flow Control Enabled by Curved Fluidic Oscillators. *AIAA J.* **2023**, *61*, 1675–1686. [CrossRef]
16. Zhao, G.; Zhao, Q.; Li, P.; Wang, B. Numerical Investigations for Passive and Active Flow Control on Tiltrotor-Wing Aerodynamic Interactions. *J. Aerosp. Eng.* **2021**, *34*, 04021094. [CrossRef]
17. Hai-long, S.; Obwogi, E.O.; Yu-min, S. Scale effects for rudder bulb and rudder thrust fin on propulsive efficiency based on computational fluid dynamics. *Ocean Eng.* **2016**, *117*, 199–209. [CrossRef]
18. Liu, J.; Hekkenberg, R. Sixty years of research on ship rudders: Effects of design choices on rudder performance. *Ships Offshore Struct.* **2017**, *12*, 495–512. [CrossRef]
19. Benedetti, D.M.; Veras, C.A.G. Wind-Tunnel Measurement of Differential Pressure on the Surface of a Dynamically Inflatable Wing Cell. *Aerospace* **2021**, *8*, 34. [CrossRef]
20. Carstensen, B.; Krüger, S. Coupling of a Boundary Element Method With a Boundary Layer Method for Accurate Rudder Force Calculation Within the Early Design Stage. In Proceedings of the 40th ASME International Conference on Ocean, Offshore and Arctic Engineering (OMAE), Electr Network, Virtual, 21–30 June 2021.
21. Lin, M.; Yang, F.; Wang, C. Numerical investigation on the generation mechanism of aero-heating of rudder shaft from three-dimensional flow separation and vortices. *AIP Adv.* **2022**, *12*, 045228. [CrossRef]
22. Abdullaev, A.; Kotvitskii, A.; Moralev, I.; Ustinov, M. On the Possibility of Cross-Flow Vortex Cancellation by Plasma Actuators. *Aerospace* **2023**, *10*, 469. [CrossRef]
23. Chen, S.; Shi, Z.; Zhao, Z.; Geng, X.; Chen, Z. Investigation of vertical tail buffeting alleviation controlled by nanosecond plasma actuators. *Phys. Fluids* **2021**, *33*, 087109. [CrossRef]
24. Manuilovich, S.V. Stability and Receptivity of the Swept-Wing Boundary-Layer Flow Controlled by a Periodic Sequence of Plasma Actuators. *Fluid Dyn.* **2021**, *56*, 630–644. [CrossRef]
25. Manuilovich, S.V. Resonance Impact of a Periodic Sequence of Plasma Actuators in Flow Control in a Swept-Wing Boundary Layer. *Fluid Dyn.* **2023**, *58*, 542–554. [CrossRef]
26. Yu, J.; Liu, H.; Xu, D.; Chen, F. Investigation of the DBD Plasma Effect on Flat Plate Flow. *Plasma Sci. Technol.* **2014**, *16*, 197–202. [CrossRef]
27. Benmoussa, A.; Páscoa, J.C. Enhancement of a cycloidal self-pitch vertical axis wind turbine performance through DBD plasma actuators at low tip speed ratio. *Int. J. Thermofluids* **2023**, *17*, 100258.
28. Omidi, J. DBD plasma actuator effect on mid-blade aerodynamics enhancement of a NREL 5-MW wind turbine. In Proceedings of the 2022 International Conference on Futuristic Technologies in Control Systems & Renewable Energy (ICFCR), Malappuram, India, 21–22 July 2022; pp. 1–6.
29. Omidi, J.; Mazaheri, K. Aerodynamic Enhancement and Improving the Performance of a Six-Megawatt DOWEC Wind Turbine by Micro-Plasma Actuator. *Int. J. Mech. Sci.* **2021**, *195*, 106228. [CrossRef]
30. Li, G.; Zhang, W.; Jiang, Y.; Yang, P. Experimental investigation of dynamic stall flow control for wind turbine airfoils using a plasma actuator. *Energy* **2019**, *185*, 90–101. [CrossRef]
31. Govindan, S.S.; Santiago, A.E.X. Optimized dielectric barrier discharge-plasma actuator for active flow control in wind turbine. *Struct. Control. Health Monit.* **2019**, *26*, e2454. [CrossRef]

32. Papadopoulos, C.; Kaparos, P.; Vlahostergios, Z.; Misirlis, D.; Yakinthos, K. 2D optimization of a Small Horizontal Axis Wind Turbine blade using flow control techniques. In *IOP Conference Series: Materials Science and Engineering, Proceedings of the 10th EASN International Conference on Innovation in Aviation & Space to the Satisfaction of the European Citizens (10th EASN 2020), Virtual, 2–4 of September 2020*; IOP Science: Bristol, UK, 2021; p. 012041.
33. Omidi, J. Advances and opportunities in wind energy harvesting using plasma actuators: A review. *Clean Energy* **2024**, *8*, 197–225.
34. Wang, X.; Yan, J.; Dhupia, J.S.; Zhu, X. Active Flow Control Based on Plasma Synthetic Jet for Flapless Aircraft. *IEEE Access* **2021**, *9*, 24305–24313. [CrossRef]
35. Almuina Pica, D.E.; Keener, K.; Lubitz, W.D. Control of Crosswind Force on Aircraft Vertical Tail Models using Plasma Actuators. In Proceedings of the AIAA Scitech 2022 Forum, San Diego, CA, USA, 3–7 January 2022; p. 0832.
36. Cai, J.; Li, C.; Li, H.; Meng, X. Design and Test of Plasma Control Surface on Unmanned Aerial Vehicle. In *The Proceedings of the 2018 Asia-Pacific International Symposium on Aerospace Technology (APISAT 2018) 9th*; Zhang, X., Ed.; Springer: Berlin/Heidelberg, Germany, 2019; pp. 1298–1311.
37. Greenblatt, D.; Schulman, M.; Ben-Harav, A. Vertical axis wind turbine performance enhancement using plasma actuators. *Renew. Energy* **2012**, *37*, 345–354. [CrossRef]
38. Chern, M.-J.; Wang, C.-C.; Wei, Z.-H.; Lu, P.-C. Numerical Investigation of a Pitching NACA 0012 Wing with Plasma-Based Flow Control Using Prediction-Correction Direct-Forcing Immersed Boundary Method. *J. Aerosp. Eng.* **2023**, *36*, 04023066. [CrossRef]
39. Chernyshev, S.; Gadzhimagomedov, G.; Kuryachiy, A.; Sboev, D.; Tolkachev, S. 3D Turbulent Boundary Layer Separation Control by Multi-Discharge Plasma Actuator. *Aerospace* **2023**, *10*, 73–85. [CrossRef]
40. Zafarghandi, F.M.; Soltani, M.R. Experimental Investigation of the Active Flow Control over a Cranked-Delta Wing. *J. Aircr.* **2024**, *61*, 73–85. [CrossRef]
41. Shyy, W.; Jayaraman, B.; Andersson, A. Modeling of glow discharge-induced fluid dynamics. *J. Appl. Phys.* **2002**, *92*, 6434–6443.
42. Zhao, Y.-J.; Zhou, Y.; Ji, K.-X.; Zhao, X.-Y.; Shao, X.; Chang, J.-L. Influence of Rudder Deflection Angle on Airfoil Lift Characteristics Under the Effect of Synthetic Jet Actuator. *J. Nanoelectron. Optoelectron.* **2021**, *16*, 1475–1484. [CrossRef]
43. Wei, B.; Wu, Y.; Liang, H.; Su, Z.; Li, Y. Flow control on a high-lift wing with microsecond pulsed surface dielectric barrier discharge actuator. *Aerosp. Sci. Technol.* **2020**, *96*, 105584. [CrossRef]
44. Abdollahzadeh, M.; Pascoa, J.C.; Oliveira, P.J. Comparison of DBD plasma actuators flow control authority in different modes of actuation. *Aerosp. Sci. Technol.* **2018**, *78*, 183–196. [CrossRef]

Disclaimer/Publisher's Note: The statements, opinions and data contained in all publications are solely those of the individual author(s) and contributor(s) and not of MDPI and/or the editor(s). MDPI and/or the editor(s) disclaim responsibility for any injury to people or property resulting from any ideas, methods, instructions or products referred to in the content.